Electronic Supplementary Information (ESI)

On-chip density-based sorting of supercooled droplets and frozen droplets in continuous flow

Grace C. E. Porter,*[a,b] Sebastien N. F. Sikora,[a] Jung-uk Shim,[b] Benjamin J. Murray[a] and Mark D. Tarn*[a,b]

[a.] *School of Earth and Environment, University of Leeds, Leeds, LS2 9JT, UK.*

[b.] *School of Physics and Astronomy, University of Leeds, Leeds, LS2 9JT, UK.*

* Email: ed11gcep@gmail.com; Tel: +44 (0) 113 343 5605.

* Email: m.d.tarn@leeds.ac.uk; Tel: +44 (0) 113 343 5605.

Contents

Additional ESI content

Video demonstrating the separation of water droplets and ice crystals in continuous flow:

ESI Video - Sorting.avi

1. Reynolds numbers and Archimedes number

The Reynolds number, Re (dimensionless), of a flowing system of fluid is the ratio of the inertial force to the viscous force, where flow in a microfluidic channel is typically considered to be laminar when Re < 2,000-2,300 (depending on the features of the system), turbulent when Re > 3,000-4,000, and transitional when 2,000 < Re < 3,000-4000 [1-3]:

$$\mathrm{Re} = \frac{\text{inertial force}}{\text{viscous force}} = \frac{\rho_\mathrm{m}\, u_\mathrm{m}\, D_\mathrm{H}}{\eta} \tag{S1}$$

where ρ_m is the density of the fluid (kg m^{-3}), u_m is the velocity of the fluid (m s^{-1}), D_H is the hydraulic diameter of the channel (m), and η is the viscosity of the fluid (kg m^{-1} s^{-1}). In the case of a very wide or tall but flat channel having a width of a and a height of b where $a \ll b$, as in the case of the microfluidic device used here, then $D_\mathrm{H} = 2a$ [4].

The Stokes' law approximation that describes the viscous force on a particle moving through a fluid (see Equation 2 in the main paper) is only valid for fluid systems in the Stokes flow regime (also known as *creeping flow*), where the Reynolds number is so low (Re << 1) that the viscous forces dominate the inertial forces [1]. In order to assess whether the Stokes' law approximation held true for our microfluidic system, the Re in the separation chamber was calculated assuming a constant temperature (−4.8 °C, which determined the values of ρ_m and η as described in Section 3 of the ESI) and flow velocity across the top ¾ of the separation chamber (to account for the approximate location of the interface between the flowing liquid and the stationary liquid at the bottom of the channel). Therefore, with an estimated channel height of 8,175 µm (the full height of the separation chamber was 10,600 µm), the fluid velocity was determined to be 2.04 mm s^{-1} based on the applied flow rates in the chip. Using these assumptions, the flow in the separation chamber was determined to have an Re = 0.4. Therefore, while this was perhaps in the upper range of the Stokes flow regime, the assumptions should hold for the use of Stokes' law as per Equation 2 in the main paper.

Also particularly pertinent to the Stokes' law assumption is the particle Reynolds number, $\mathrm{Re_p}$ (dimensionless), which describes the flow of fluid around a particle [5,6]:

$$\mathrm{Re_p} = \frac{\text{inertial force}}{\text{viscous force}} = \frac{\rho_\mathrm{m}\, u_\mathrm{p}\, D_\mathrm{p}}{\eta} \tag{S2}$$

where D_p is the particle diameter (m), and u_p is the velocity of the particle (m s^{-1}), either in the x-direction as the velocity due to the hydrodynamic flow, $\boldsymbol{u}_\mathbf{hyd}$, or in the y-direction as the velocity due to the particle's buoyancy, $\boldsymbol{u}_\mathbf{buoy}$. $\mathrm{Re_p}$ was calculated for both $\boldsymbol{u}_\mathbf{buoy}$ and $\boldsymbol{u}_\mathbf{hyd}$ using the average velocity values and particle diameters for the experimental runs in each case, as shown in Table S1.

Table S1 The particle Reynolds numbers, $\mathrm{Re_p}$ (dimensionless), determined for water droplets and ice crystals in the x-direction and y-direction in the microfluidic separation chamber, based on the experimentally determined particle velocities and diameters.

	$\mathbf{Re_p}$	
	x-direction ($\boldsymbol{u}_{\mathbf{hyd}}$)	**y-direction ($\boldsymbol{u}_{\mathbf{buoy}}$)**
Water droplets	0.15	0.05
Ice crystals	0.17	0.06

Stokes' law holds true for $\mathrm{Re_p}$ < 0.2-1 [5,6], and as $\mathrm{Re_p}$ exceeds 1 the theory begins to deviate from experimental data [6]. In our system, the water droplets and ice crystals demonstrated $\mathrm{Re_p}$ < 0.2 in both the x- and y-directions, further indicating that the use of Stokes' law in Equation 2 is appropriate. Most importantly, the $\mathrm{Re_p}$ value in the y-direction due to $\boldsymbol{u}_{\mathbf{buoy}}$ was much smaller than 0.2, and this is the relevant quantity regarding the use of Equations 1 and 2 in the main paper to describe the sedimentation or creaming of a particle due to gravity.

Additionally, the settling regime of our system can be described by the Archimedes number, Ar (dimensionless). Ar is defined in a similar manner as $\mathrm{Re_p}$, in that it describes a force encouraging particle movement against a force resisting that movement, but is more specifically for the vertical movement of a particle in that it is the ratio between the sinking force (the particle's weight minus its buoyancy) and the viscous force [7,8]:

$$\mathrm{Ar} = \left(\frac{\text{sinking force}}{\text{viscous force}}\right)^2 = \frac{\rho_\mathrm{m}\,(\rho_\mathrm{p}-\rho_\mathrm{m})\,g\,(D_\mathrm{p})^3}{\eta^2} \tag{S3}$$

where ρ_p is the density of the particle (kg m^{-3}) and g is the acceleration due to gravity (9.81 m s^{-2}). An Ar < 32.9 places the particle in fluid in the Stokes regime, the intermediate regime is 32.9 < Ar < 106,520, and Ar > 106,520 is the Newton regime [7]. Equation 3 in the main paper, which describes the sedimentation/creaming velocity ($\boldsymbol{u}_{\mathbf{buoy}}$) of a particle in a fluid, can only be used in its presented form when the particle is in the Stokes regime. In our system, the Ar values of the water droplets and ice crystals were calculated to be 3.8 and 4.6, respectively, hence they were in the Stokes regime and so Equation 3 holds true for the calculation of $\boldsymbol{u}_{\mathbf{buoy}}$.

2. Viscous drag coefficient, C_W

The viscous drag coefficient, C_W (dimensionless), describes the effect of viscous drag experienced by particles due to the surfaces of a microchannel through which they flow, and can be calculated using Equation S4 [9-11]:

$$C_W = \left[1 - 1.004\left(\frac{r}{h_z}\right) + 0.418\left(\frac{r}{h_z}\right)^3 + 0.21\left(\frac{r}{h_z}\right)^4 - 0.169\left(\frac{r}{h_z}\right)^5\right]^{-1} \quad \text{(S4)}$$

where r is the particle radius (m), and h_z is half the distance of the shortest dimension of the microchannel (m). In this case, the shortest dimension of the microfluidic separation chamber was its width of 140 µm, hence h_z was 7×10^{-5} m. C_W was calculated for experimentally measured radii of the water droplets (average radius = 59.2 µm) and ice crystals (average radius = 60.9 µm), yielding a C_W value of 2.28 for the water droplets and ice crystals.

3. Properties of Novec™ 7500 Engineered Fluid

The absolute (dynamic) viscosity, η (kg m^{-1} s^{-1}; Pa s; Poise), of the 3M™ Novec™ 7500 Engineered Fluid (2-trifluoromethyl-3-ethoxydodecafluorohexane; $C_7F_{15}OC_2H_5$; CAS No. 297730-93-9) was calculated from the kinematic viscosity, ν_k (m^2 s^{-1}), and the density, ρ_m (kg m^{-3}), of the fluid at temperature T (°C) using Equation S5:

$$\eta = \nu_k \, \rho_m \tag{S5}$$

The kinematic viscosity, ν_k (m^2 s^{-1}), of the fluid temperature T (°C) inside the separation chamber of the microfluidic device was determined using Equations S6 and S7, which were adapted from the manufacturer's product information [12]:

$$\begin{aligned}\nu_k = [(Z - 0.7) - \exp(-0.7487 - 3.295(Z - 0.7) \\ +0.6119(Z - 0.7)^2 - 0.3193(Z - 0.7)^3)] \times 10^{-6}\end{aligned} \tag{S6}$$

where

$$Z = 10\hat{}(10^{11.843 - 5.0874 \log(T + 273.15)}) \tag{S7}$$

The density, ρ_m (kg m^{-3}), of the Novec™ 7500 Engineered Fluid at temperature T (°C) was calculated using Equation S8, obtained from the manufacturer's product information [12]:

$$\rho_m = -2.0845 \, T + 1665.8 \tag{S8}$$

The changes in viscosity and density of Novec™ 7500 Engineered Fluid with decreasing temperature below 0 °C are shown in Fig. S1 and Fig. S2, respectively.

4. Viscosity of supercooled water

Although the calculation of the viscosity of supercooled water was not needed for any calculations related to the droplet sorting experiments, it was of general interest and is useful to compare to the viscosity of the Novec™ 7500 Engineered Fluid. The viscosity of water, η_w (kg m^{-1} s^{-1}), at temperature T (K) was calculated using the parameterisation of Dehaoui et al. [13], which both fit well with and extended the datasets of Hallett [14], Collings and Bajenov [15], and Osipov et al. [16], as shown in Equation S9.

$$\eta_{\mathrm{w}} = \eta_0 \left(\left(\frac{T}{T_s} \right) - 1 \right)^{-\gamma} \tag{S9}$$

where η_0 = 1.38 × 10^{-4} kg m^{-1} s^{-1}, T_s = 225.66 K, and γ = 1.6438.

The viscosity of supercooled water at sub-zero temperatures (calculated using Equation S9) was compared to that of the Novec™ 7500 Engineered Fluid (calculated using Equations S5-S8), which highlighted the small response to changes in temperature of the Novec™ 7500 compared to supercooled water (Fig. S1).

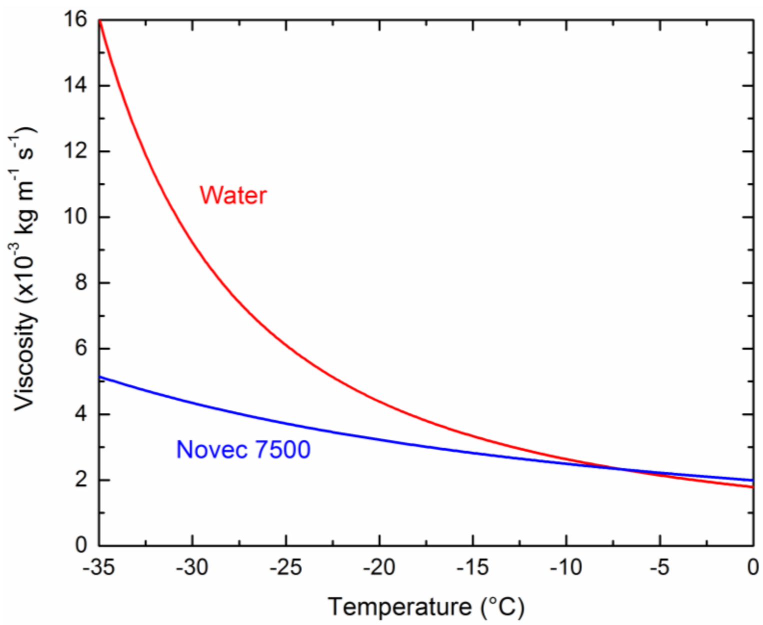

Fig. S1 The change in viscosity at sub-zero temperatures for Novec™ 7500 Engineered Fluid and supercooled water.

5. Density of supercooled water

The density of water, ρ_w (g cm^{-3}), at temperature T (°C) below 0 °C was calculated using the parameterisation of Hare and Sorensen [17], whose values are used in the *CRC Handbook of Chemistry and Physics* [18], as shown in Equation S10. The ρ_w values were then converted to kg m^{-3} in later calculations and these values can be seen in Fig. S2.

$$\rho_{\mathrm{w}} = \sum_{n=0}^{6} a_n T^n \tag{S10}$$

where the a_n constants are as follows:

a_0 = 0.99986

a_1 = 6.690×10^{-5}

a_2 = -8.486×10^{-6}

a_3 = 1.518×10^{-7}

a_4 = -6.9484×10^{-9}

a_5 = -3.6449×10^{-10}

a_6 = -7.497×10^{-12}

6. Density of ice

The density of ice, ρ_i (g cm^{-3}), at temperature T (°C) was calculated using the parameterisation of Pruppacher and Klett [19], as shown in Equation S11, which is based on a fit of the data from La Placa and Post [20], Ginnings and Corruccini [21], and Lonsdale [22]. As such, it effectively also represents a fit of the ρ_i values in the *CRC Handbook of Chemistry and Physics* [18], which were taken from Eisenberg and Kauzmann [23] based on their computation of the X-ray diffraction data of La Placa and Post [20]. The ρ_i values calculated using Equation S11 were later converted to kg m^{-3} for subsequent calculations.

$$\rho_\mathrm{i} = \sum_{n=0}^{2} a_n T^n \quad \text{(S11)}$$

where the a_n constants are as follows:

a_0 = 0.9167

a_1 = -1.75×10^{-4}

a_2 = -5.00×10^{-7}

A comparison of the differences in density for Novec™ 7500 Engineered Fluid, water, and ice over a range of temperatures below 0 °C is shown in Fig. S2, based on calculations using Equations S8, S10, and S11, respectively.

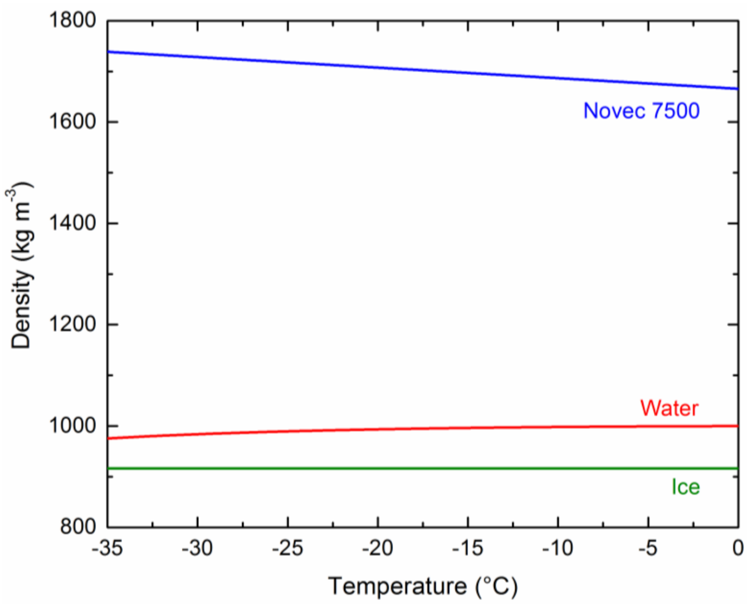

Fig. S2 The densities of Novec™ 7500 Engineered Fluid, water, and ice at sub-zero temperatures.

7. Theoretical F_{buoy} and u_{buoy} values

Theoretical values for the buoyancy force, F_{buoy}, and the velocity in the y-direction of the microfluidic separation chamber due to the buoyancy, u_{buoy}, were calculated for liquid water droplets and ice crystals using Equations 1-3 from the main paper. Viscosity and density values for the calculations were obtained using Equations S5-S8, S10, and S11 for Novec™ 7500 Engineered Fluid, water, and ice, and a nominal water droplet diameter of 115 μm (equivalent to 796 pL) was selected. The change in F_{buoy} with temperature for water droplets and ice crystals is shown in Fig. S3a, and demonstrates the greater buoyancy forces on the ice crystals across the full temperature range of 0 to −35 °C. The difference in F_{buoy} between the water droplets and ice crystals (ΔF_{buoy}) is shown in Fig. S3b. This effect is further reflected in the u_{buoy} values, shown in Fig. S4a, which used the viscous drag coefficient, C_w, calculated as described in Equation S4 for the microfluidic separation chamber. This shows an increase in the u_{buoy} velocity of ice crystals in the y-direction of the separation chamber compared to the water droplets, illustrated in Fig. S4b as the difference in velocities (Δu_{buoy}) between the ice crystals and water droplets. The differences in F_{buoy} and u_{buoy} between the water droplets and ice crystals provide the means by which the two species can be separated in continuous flow. The F_{buoy} and u_{buoy} values for water and ice are actually negative, indicating that they would each cream rather than sediment with respect to gravity, but are shown in Figs. S3 and S4 as positive values for simplicity.

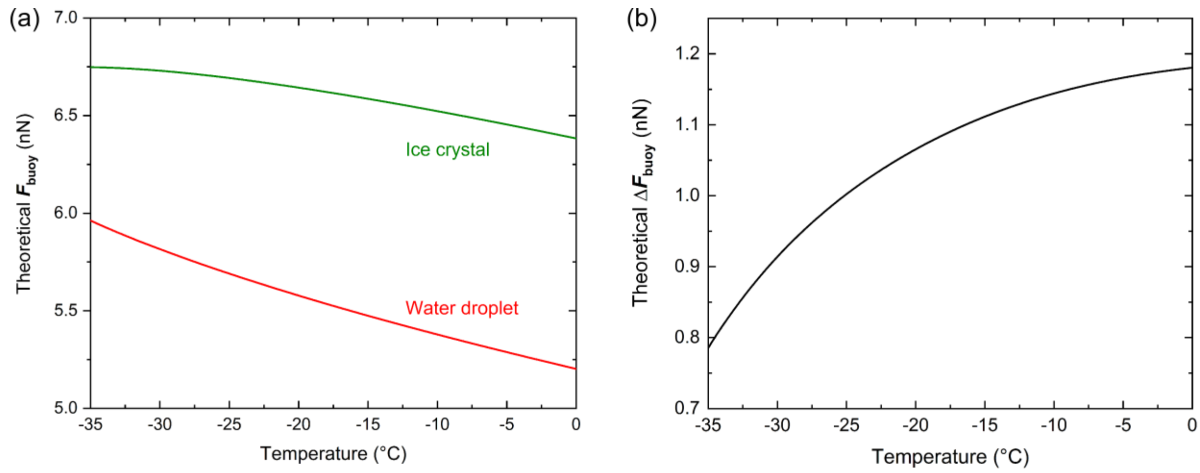

Fig. S3 (a) The temperature-dependent change in theoretical buoyancy force in the y-direction, $\boldsymbol{F}_{\mathbf{buoy}}$, for a water droplet of 115 μm nominal diameter and an ice crystal (117.2-118.4 μm diameter depending on the temperature, based on the volume increase upon the freezing of a 115 μm water droplet) in Novec™ 7500 Engineered Fluid. (b) The difference in $\boldsymbol{F}_{\mathbf{buoy}}$ between a water droplet and an ice crystal in Novec™ 7500 Engineered Fluid, based on the parameters in (a).

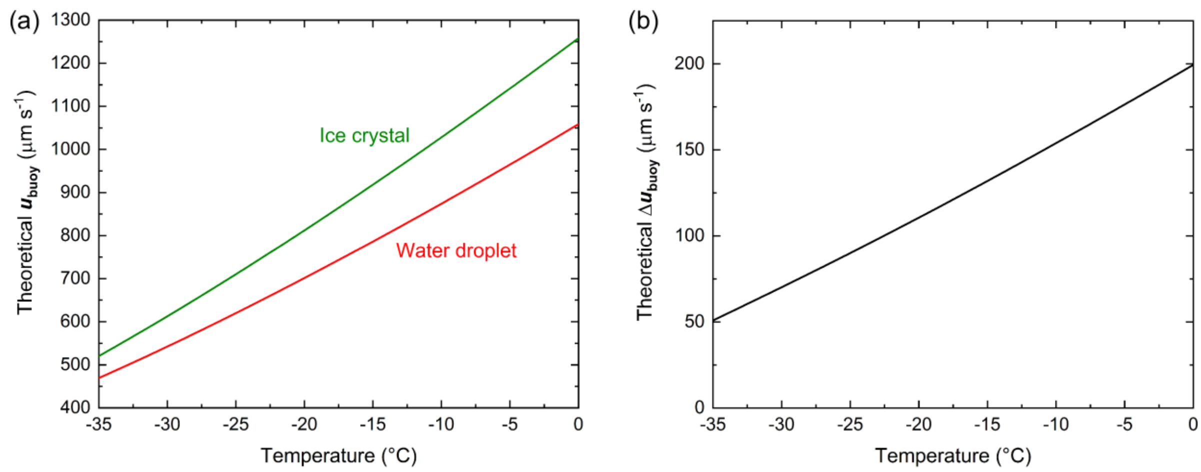

Fig. S4 (a) The temperature-dependent change in the theoretical velocity in the y-direction, $\boldsymbol{u}_{\mathbf{buoy}}$, of a water droplet (115 μm nominal diameter) and an ice crystal (117.2-118.4 μm diameter depending on the temperature) in Novec™ 7500 Engineered Fluid. (b) The difference in $\boldsymbol{u}_{\mathbf{buoy}}$ between a water droplet and an ice crystal in Novec™ 7500 Engineered Fluid, based on the parameters in (a).

8. Fabrication and setup of the microfluidic device

8.1 Fabrication of the microfluidic device

The fabrication of the microfluidic device was performed as described by Tarn et al. [24], using standard soft lithography procedures [24-26]. The chip design (see Fig. 1c in the main paper) was prepared using AutoCAD 2017 software (Autodesk, Inc., San Rafael, CA, USA), from which an emulsion-on-film photomask was printed by JD Photo Data (Hitchin, UK). A 140 μm thick layer of MicroChem SU-8 2075 negative photoresist (A-Gas Electronic Materials Ltd., Rugby, UK) was spin-coated onto a silicon wafer (3" diameter, PI-KEM Ltd., Tamworth, UK) and baked on. The wafer was then exposed to ultraviolet (UV) light (210 mJ cm^{-2}) through the film photomask using a mask aligner (Model 200, OAI). Following another baking step, the wafer was developed in photodeveloper solution (Microposit EC Solvent Developer, A-Gas Electronic Materials Ltd.), rinsed with isopropanol (Fisher Scientific, Loughborough, UK) and dried with nitrogen gas. The final SU-8 structure of the microfluidic design on the silicon wafer was then profiled using a surface profiler (Dektak XT, Bruker), with the final thickness of the SU-8 structures being 140 ± 5 μm in height.

Poly(dimethylsiloxane) (PDMS, Dow Corning® Sylgard® 184 Kit, Ellsworth Adhesives, East Kilbride, UK) was mixed in a 10:1 ratio of base elastomer to curing agent and poured onto the silicon wafer, before being degassed in a vacuum desiccator for 1-2 h and finally allowed to cure at 75 °C for 1 h. The PDMS was then peeled off the silicon wafer and the microfluidic chips cut out using a scalpel. Access holes (1 mm Ø) were punched into the PDMS devices, which were then bonded to glass microscope slides (76 x 26 x 1 mm^3, Academy Science Products, Kent, UK) following plasma treatment (Zepto Version B, Diener Electronic GmbH, Germany) and allowed to cure at 75 °C for 1 h (see Fig. 2a in the main paper).

8.2 Setup and operation of the microfluidic device

Polyethylene tubing (Smiths Medical, 0.38 mm inner diameter (i.d.) × 1.09 mm outer diameter (o.d.), Harvard Apparatus, Biochrom Ltd., Cambridge, UK) was inserted into the inlet and outlet access holes of the PDMS microfluidic device (see Fig. 2a in the main paper). The inlet tubing had syringe needles (26 G x 23 mm, Terumo Neolus®, VWR, Lutterworth, UK) inserted into their opposite ends to allow their connection to glass syringes (SGE, Sigma-Aldrich, UK), which were inserted into separate syringe pumps (PHD Ultra, Harvard Apparatus, Biochrom Ltd.). An aqueous sample of 0.01 % w/w Snomax® Snow Inducer (Snomax International, purchased from SMI Snow Makers AG, Thun, Switzerland), a non-viable lyophilised form of *Pseudomonas syringae* bacteria, in a 1 mL glass syringe was pumped into the aqueous inlet channel at a flow rate of 0.1 μL min^{-1} for droplet generation. A solution of 0.2 % w/w

Pico-Surf™ 1 surfactant (prepared from a stock concentration of 5 % w/w, Sphere Fluidics Ltd., Cambridge, UK) in 3M™ Novec™ 7500 Engineered Fluid (Fluorochem Ltd., Hadfield, UK) in a 1 mL glass syringe was pumped into the droplet generation oil inlet at a flow rate of 25 μL min^{-1} for the production of droplets. Novec™ 7500 Engineered Fluid, without the addition of surfactant, was pumped into the upper control flow inlet of the separation chamber at a flow rate of 113-115 μL min^{-1}. A 1 mL syringe containing Novec™ 7500 Engineered Fluid was connected to the lower control flow inlet of the separation chamber and was used to assist in the flushing of the chamber with Novec™ 7500, but was thereafter not used although it remained in place on the syringe pump to prevent fluctuations in the flow regime from that inlet. The three outlet tubes connected to the outlet access holes of the separation chamber were fed into a waste vial containing a small amount of Novec™ 7500.

8.3 Setup of the cold stage platform

The microfluidic device, with the tubing connected, was turned sideways and inserted into a cold stage platform that had been also been turned sideways, such that the wide separation chamber was now oriented vertically (see Fig. 2b in the main paper). The construction and operation of the cold stage platform and its associated temperature control unit are described in detail by Tarn et al. [24]. Briefly, the cold stage platform comprised three Peltier elements housed within a 3D printed body. Aluminium liquid heat exchangers located beneath each Peltier element allowed the flow of coolant (polyethylene glycol in water) through the system via a refrigerated recirculating chiller (WK 500, Lauda, UK) that was set to +5 °C. Polished aluminium plates were set upon each Peltier element and featured access holed that allowed the insertion of thermocouples. The Peltier elements and thermocouples were connected to a custom-built, four-channel temperature control unit based on an Arduino Nano microcontroller (purchased from RS Components, Northants, UK) and bidirectional motor drivers (IBT_2 BTS7960 43A High Power Motor Driver) controlled via a pulse width modulation (PWM) driver (PCA9685, Adafruit Industries, USA) that allowed the temperature of the aluminium plates to be controlled using a proportional-integral-derivative (PID) loop written in Python (Python Software Foundation, Delaware, USA). The electronics package in the temperature control unit featured improvements over the previous version used by Tarn et al. [24], with the wiring layout now integrated onto a printed circuit board (PCB; fabricated by Seeed Technology Co. Ltd., Shenzhen, People's Republic of China), as shown in Fig. S5, rather than the hand-wired breadboard previously used, and featuring a universal serial bus (USB) isolator to reduce signal noise and interference.

The three aluminium plates were located in serial such that the microfluidic chip lay across all three, allowing the first plate (37 mm × 33 mm) to control the temperature of the droplet generation region of the chip (at a setpoint of +3 °C), the middle plate (8 mm × 14 mm) to allow the freezing of water-in-oil droplets in the main channel (at a setpoint of −17 °C), and the final plate (37 mm × 33 mm) to control the temperature of the separation chamber (at a setpoint of −8 °C). Whilst the previous version of the cold stage platform had required the underside of the microfluidic chips to be coated with a layer of chromium to aid visualisation via reflected light microscopy [24], here the aluminium plates were polished to render them reflective enough that chromium-coating of the chips was no longer required.

The chip was held in place in the cold stage platform using clips, and a Perspex lid was placed on the stage to form a chamber around the chip, with the tubing fed through access holes to the syringe pumps and waste vials outside the chamber. The chamber was purged with compressed air that had been passed through a drying unit in order to remove moisture that would otherwise condense onto the chip upon cooling to sub-zero temperatures. A modular Navitar Zoom 6000® Lens System (Mengel Engineering, Denmark) with coaxial lighting provided by an OPT Machine Vision 3 W light-emitting diode (LED) light source (Mengel Engineering) ws used for visualisation of water droplets and ice crystals inside the microfluidic device. A Phantom Miro Lab 120 high-speed camera with PCC 2.7 software (Vision Research Ltd., Bedford, UK) connected to the Navitar Zoom 6000® Lens System was used to record videos and take images of droplet/crystal separations at a frame rate of 25 fps. A photograph of the complete setup is shown in Fig. S6, while a close-up photograph of a microfluidic chip positioned over the three cold stage plates in the chamber of the platform can be seen in Fig. 2b in the main paper.

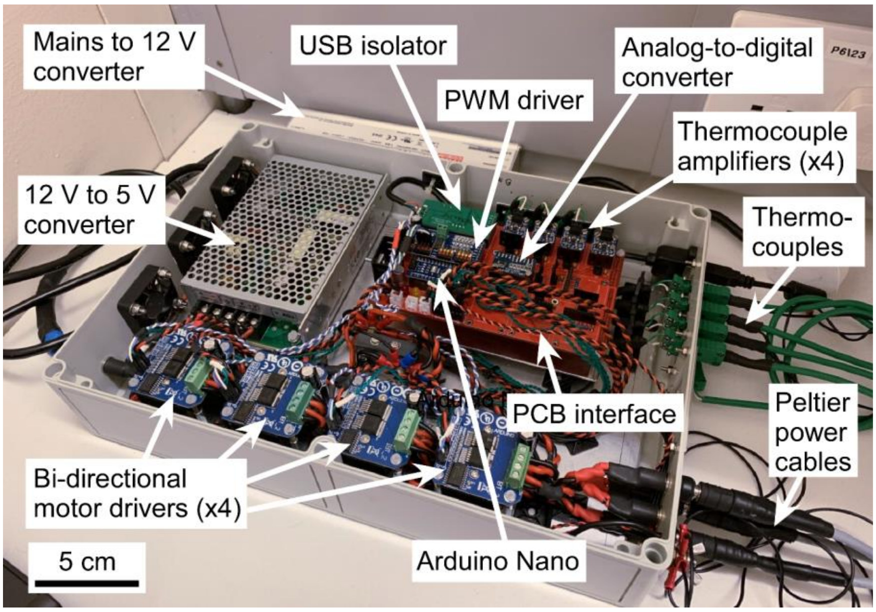

Fig. S5 Photograph of the updated electronics package of the temperature control unit used to power the Peltier elements in the cold stage platform. The new package included a printed circuit board (PCB) that contained the wiring layout, compared to the hand-wired breadboard of the previous platform [24], and also featured a USB isolator to reduce electrical noise and interference.

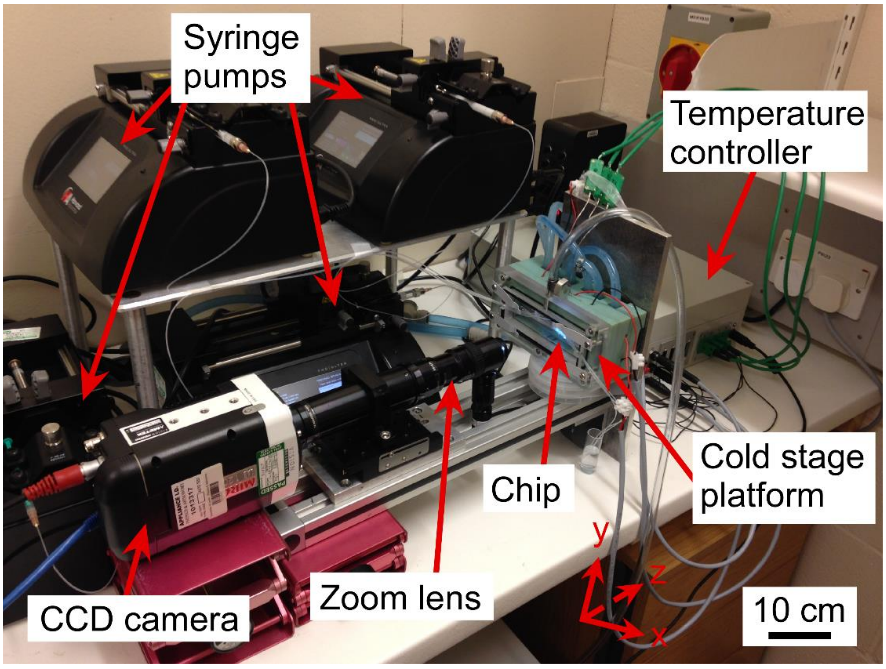

Fig. S6 Photograph of the apparatus used to perform the continuous flow separation of liquid water droplets and ice crystals in a microfluidic device. The photograph highlights the cold stage platform in which the microfluidic chip was placed, the temperature control unit, syringe pumps, and the visualisation setup. The recirculating chiller used to pump coolant through the cold stage platform is out of shot, and was located beneath the bench.

9. On-chip temperature measurements

On-chip temperature measurements of the Novec™ 7500 Engineered Fluid as it flowed through the microfluidic separation chamber were performed in order to inform calculations of $\boldsymbol{F}_{\mathbf{buoy}}$ and $\boldsymbol{u}_{\mathbf{buoy}}$, which incorporate the temperature-dependent fluid viscosity (η) and density (ρ). The procedure was performed in a similar fashion to that described by Tarn et al. [24]. Two access holes (1 mm Ø) were punched into the chamber of the PDMS chip, one in the centre of the separation chamber and one above it (approximately ¾ of the way up the chamber), prior to bonding the PDMS to a glass microscope slide. After bonding, the access holes allowed the insertion of two thermocouples (80 µm diameter, 5SRTC-TT-KI-40-1M series K-type, Omega Engineering Ltd., Manchester, UK) into the chamber, as shown in Fig. S7.

The thermocouples were connected to a data logger (TC-08, ±0.025 °C, Pico Technology, St. Neots, UK), and had been calibrated against a platinum resistance thermometer (PRT; Netushin NR-141-N L10, RS Components, UK) connected to a custom-built Arduino-based temperature logger. This PRT, in turn, had been calibrated against a high-precision PRT probe (Model 5608, ±0.0013 °C, Fluke Corporation, USA) and temperature logger (Model 1560, Fluke Corporation, USA) that had been calibrated by the National Physical Laboratory (NPL, Teddington, UK). Following calibration, the thermocouples were estimated to have an uncertainty of ±0.03 °C in their readings. Short sections of polyethylene tubing (0.38 mm i.d. × 1.09 mm o.d., Smiths Medical) were used as sleeves around the thermocouple wires and sealed with glue, allowing the thermocouples to be inserted easily into the access holes of the chip via the sleeves without any leakage.

Temperature measurements in the separation chamber were taken under the same operating conditions (i.e. flow rates and cold stage plate temperatures) as were used in droplet separation experiments, albeit with only Novec™ 7500 Engineered Fluid being pumped into the chip (i.e. no aqueous sample, hence no droplets were formed during temperature measurements). The logged temperatures were corrected according to their calibration factors at each operating parameter, and the two temperature readouts (for the middle and top of the separation chamber) were averaged to obtain a typical temperature value for the chamber.

The variation in temperature in the measured region of the chamber under the operating conditions was no greater than 0.05 ± 0.03 °C, and this variation was largely caused by the duty cycle of the refrigerated recirculating chiller that was used to pump coolant through the cold stage platform. The difference in temperature between the two thermocouples was 0.07 ± 0.07 °C at its greatest. At a separation cool plate set temperature of −8 °C, the temperature inside the measured region of the chamber was −4.8 ± 0.2 °C, and this was used to calculate experimental $\boldsymbol{F}_{\mathbf{buoy}}$ values from the experimental $\boldsymbol{u}_{\mathbf{buoy}}$, in addition to being used to calculate theoretical $\boldsymbol{F}_{\mathbf{buoy}}$ and $\boldsymbol{u}_{\mathbf{buoy}}$ values for comparison. However, these calculations were made with the caveat that the temperature measurements taken at specific locations in the chamber were used to represent the chamber as a whole, while the temperatures at different parts of the chamber likely varied due to the multiple sources of fluids at different flow rates and temperatures entering the chamber.

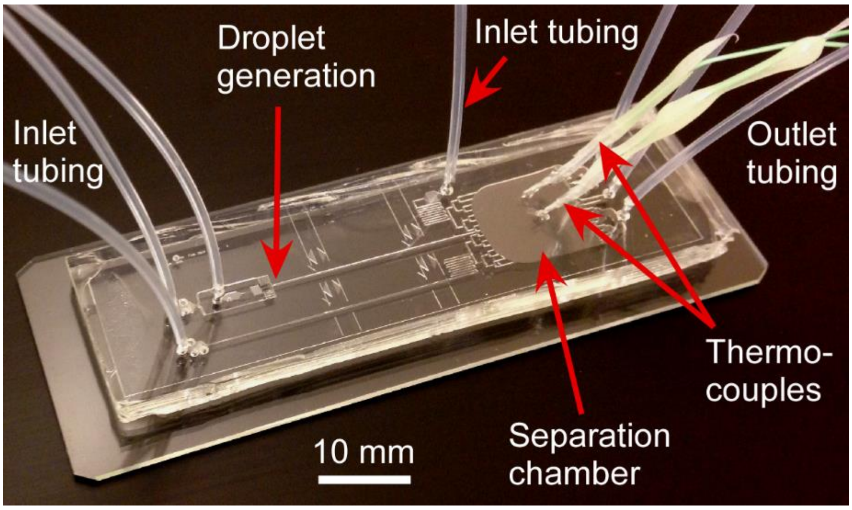

Fig. S7 Setup of the microfluidic chip for on-chip temperature measurements of the Novec™ 7500 Engineered Fluid as it flowed through the separation chamber. Two K-type thermocouples were inserted into the chamber, one at the midpoint and one slightly above it, and the two readings were averaged to indicate the temperature in the chamber where the water droplets and ice crystals would pass.

10. Properties of low viscosity silicone oil

The properties of low viscosity silicone oil (kinematic viscosity of 5 cSt at 25 °C) were explored theoretically as a potential means of improving the separation of water droplets and ice crystals in future iterations of the microfluidic sorting platform. Kamijo and Derda [28] used a low viscosity silicone oil, DM-FLUID-5cs (polydimethylsiloxane (PDMS); $(C_2H_6OSi)_n$) from Shin-Etsu Chemical Co., Ltd., containing 1 % v/v KF-6017 silicone-based emulsifier (Shin-Etsu Chemical Co., Ltd.) to assist in their static, cuvette-based method of separating water droplets and ice crystals (1 μL volume, ≈1.24 mm diameter) via buoyancy forces. Their system comprised a cushion fluid of Novec™ 7500 Engineered Fluid beneath a layer of DM- FLUID-5cs silicone fluid. Water droplets, having a density between the Novec™ 7500 and DM- FLUID-5cs, remained at the biphasic interface between the two fluids, but when droplets froze the resultant ice crystals had a density lower than both fluids, causing them to float to the top of the silicone oil and thus achieving separation.

This strategy could potentially be adapted to the continuous flow microfluidic sorting platform by pumping a low viscosity silicone oil, such as DM-FLUID-5cs, into the top of the separation chamber instead of Novec™ 7500, as illustrated in Fig. S8. Assuming the ice crystals could cross the interface from the Novec™ 7500 into the silicone oil (surface tension of DM-FLUID-5cs = 19.7 mN m^{-1} at 25 °C [29]), which may require the addition of a surfactant such as KF-6017 in the silicone oil phase, then the ice crystals could continue to migrate through the silicone oil in the y-direction whilst the water droplets would be unable to pass into the silicone oil and so remain at the same height throughout the chamber, thus potentially increasing the separation distances and efficiencies.

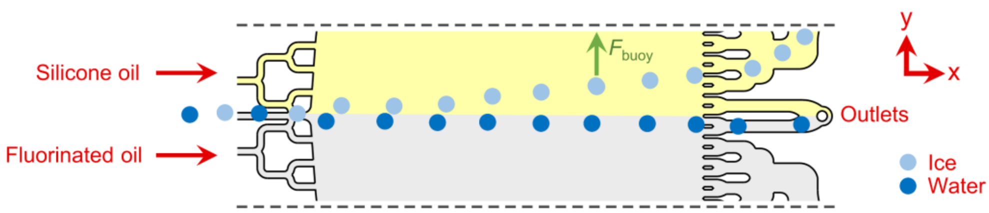

Fig. S8 Schematic showing the principle of employing a low viscosity silicone oil as the upper control flow in the separation chamber of the microfluidic device. Here, water droplets would be unable to pass from the Novec™ 7500 Engineered Fluid into the silicone phase due to their being denser than the silicone oil, thereby providing a barrier to their migration in the y-direction. Ice crystals, on the hand, would have a lower density than the silicone oil and so would continue to travel in the y-direction, thus achieving separation.

In a similar manner to above, in which the theoretical $\boldsymbol{F}_{\mathbf{buoy}}$ and $\boldsymbol{u}_{\mathbf{buoy}}$ values of water droplets and ice crystals in Novec™ 7500 Engineered Fluid were calculated, here the theoretical values for water and ice in DM-FLUID-5cs, as a representative low viscosity silicone oil, were calculated based on data provided by the manufacturer [29]. The technical data sheet only provides a handful of data points for the kinematic viscosity and density of the silicone fluid below 0 °C, and not always at corresponding temperatures, but these data points were used to calculate the absolute viscosity for a limited number of temperatures using Equation S5. Fits were then applied to the available data points in order to approximate the absolute viscosity, η_s, and density, ρ_s, of DM-FLUID-5cs over a temperature range of 0 to −35 °C.

An Arrhenius-type equation was generated for the absolute viscosity, η_s, by first plotting the available data in terms of ln(η_s) vs $1/T$, with temperature in units of K, in order to obtain parameters for A (from the intercept) and B (from the slope). Thus, η_s (kg m^{-1} s^{-1}) could be calculated for temperature T (K) as shown in Equation S12:

$$\eta_{\mathrm{s}} = A\ \mathrm{e}^{B/T} \tag{S12}$$

where A = 7.935 × 10^{-6} kg m^{-1} s^{-1}, and B = 1889.608 K. A plot of DM-FLUID-5cs viscosities calculated using Equation S12 is shown in Fig. S9a alongside the viscosities of water and Novec™ 7500.

A linear fit was applied to the available density data, ρ_s (kg m^{-3}), for the DM-FLUID-5cs fluid for temperature T (°C), as shown in Equation S13:

$$\rho_s = -0.98237\,T + 939.8938 \tag{S13}$$

A plot of the DM-FLUID-5cs density calculated using Equation S13 is shown in Fig. S9b alongside the densities of water, ice, and Novec™ 7500, and clearly demonstrates how the density of a low viscosity silicone oil such as DM-FLUID-5cs sits between the densities of water and ice for the temperature range shown.

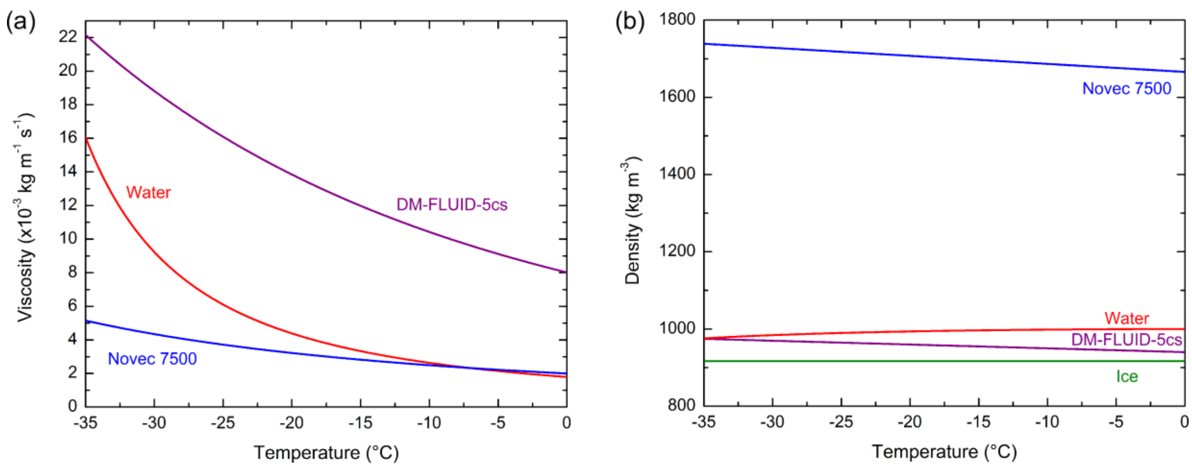

Fig. S9 The properties of DM-FLUID-5cs, as a representative low viscosity silicone oil, calculated by fitting the data provided by the manufacturer [29]. (a) The viscosity, η_s, of DM-FLUID-5cs with temperature, and (b) the density, ρ_s, of DM-FLUID-5cs with temperature. The values of water, ice, and Novec™ 7500 Engineered Fluid are shown for comparison, using the data from Figs. S1 and S2.

The calculated η_s and ρ_s values were used to estimate the $\boldsymbol{F}_{\mathbf{buoy}}$ and $\boldsymbol{u}_{\mathbf{buoy}}$ values of ice crystals and water droplets in DM-FLUID-5cs using Equations 1-3 in the main paper, assuming an initial water droplet diameter of 115 μm that would yield ice crystals of 117.2-118.4 μm. depending on the temperature). The $\boldsymbol{F}_{\mathbf{buoy}}$ results are shown in Fig. S10a, while the differences between the ice crystals and water droplets, $\Delta\boldsymbol{F}_{\mathbf{buoy}}$, are shown in Fig. S10b, with the results for ice crystals and water droplets in Novec™ 7500 also shown for comparison. The results in Fig. S10 demonstrate that the $\boldsymbol{F}_{\mathbf{buoy}}$ forces in DM-FLUID-5cs are orders of magnitude lower than in Novec™ 7500, and, importantly, even the $\Delta\boldsymbol{F}_{\mathbf{buoy}}$ values between a water droplet and ice crystal are much smaller in DM-FLUID-5cs compared to Novec 7500™. Notably, the $\boldsymbol{F}_{\mathbf{buoy}}$ values for a water droplet in DM-FLUID-5cs are below 0 nN, thus reaffirming that water droplets would sediment in DM-FLUID-5cs.

Similar trends can be seen in the $\boldsymbol{u}_{\mathbf{buoy}}$ values for water droplets and ice crystals, as shown in Fig. S11a, together with the $\Delta\boldsymbol{u}_{\mathbf{buoy}}$ values between the two shown in Fig. S11b. The results show that the water droplets and ice crystals would move far more slowly in DM-FLUID-5cs compared to being in Novec™ 7500, and the $\Delta\boldsymbol{u}_{\mathbf{buoy}}$ values in DM-FLUID-5cs would be far smaller than in Novec™ 7500, due to both the smaller $\Delta\boldsymbol{F}_{\mathbf{buoy}}$ and the high viscosity of DM-FLUID-5cs. The water droplets are shown as having a velocity below 0 μm s^{-1}, indicating that they would sediment in the y-direction rather than creaming when suspended in DM-FLUID-5cs, but in the context of the proposed experiment (see Fig. S8), the water droplets would not be able to enter the silicone phase in the first place based on their respective densities.

Therefore, even given the fact that in a continuous sorting system the water droplets should be unable to cross into the silicone phase, the velocity of the ice crystals in the y-direction in the silicone oil may be too low (up to 8 μm s^{-1}) to achieve a better separation than when only using Novec™ 7500, or to achieve a reasonable separation at all, at least without changes to the chip and the method. For example, the silicone oil flow rate could be greatly decreased in order to provide much longer residence times of the ice crystals in the separation chamber, thus allowing the crystals to migrate further in the y-direction, although this would impact on the throughput. A further issue could be that, given that the current microfluidic device is prepared from PDMS, there may also be issues with trying to use a PDMS fluid in the chip, though this could be alleviated by fabricating the device from other materials. Thus, although the use of silicone oil to enable a separation, as envisaged in Fig. S8, may be a viable strategy, further work would be required to ensure that ice crystals could migrate far enough in the y-direction to achieve a separation given the low $\boldsymbol{u}_{\mathbf{buoy}}$ velocities. Given this, continuing to use Novec™ 7500 as the only oil in the system is likely still the better strategy for the platform going forward.

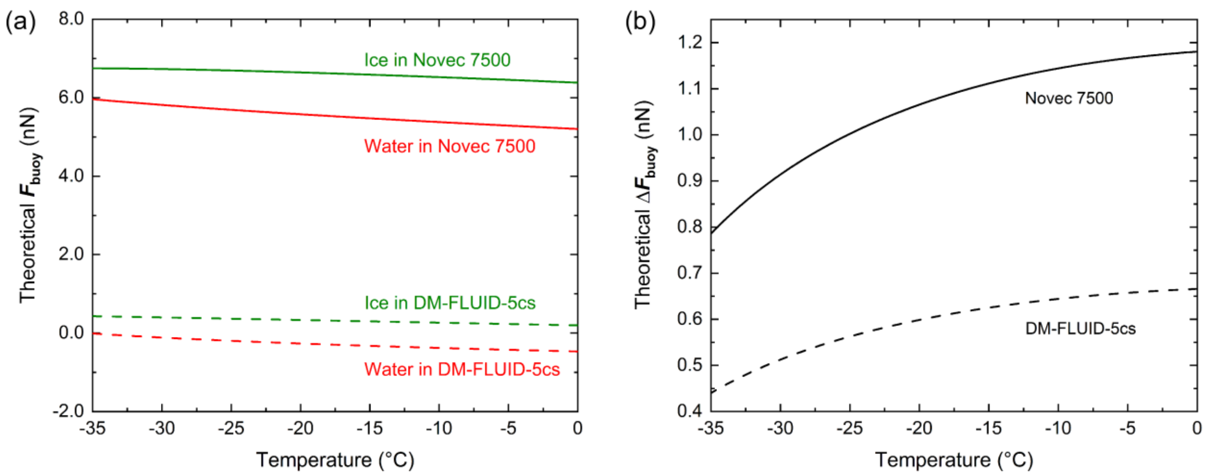

Fig. S10 (a) The theoretical buoyancy forces, $\boldsymbol{F}_{\mathbf{buoy}}$, on a water droplet and an ice crystal in Novec™ 7500 Engineered Fluid fluorinated oil (solid lines) and DM-FLUID-5cs low viscosity silicone oil (dashed lines). The water droplet was assumed to have a diameter of 115 μm, while the ice crystal had a temperature-dependent diameter of 117.2-118.4 μm based on the freezing of a 115 μm diameter water droplet. The negative values for the water droplets in DM-FLUID-5cs indicate that the droplets would sediment in this silicone oil phase instead of creaming. The data for water and ice in Novec™ 7500 are the same as shown in Fig. S3. (b) The difference in theoretical $\boldsymbol{F}_{\mathbf{buoy}}$ values between a water droplet and ice crystal in Novec™ 7500 Engineered Fluid fluorinated oil and DM-FLUID-5cs silicone oil.

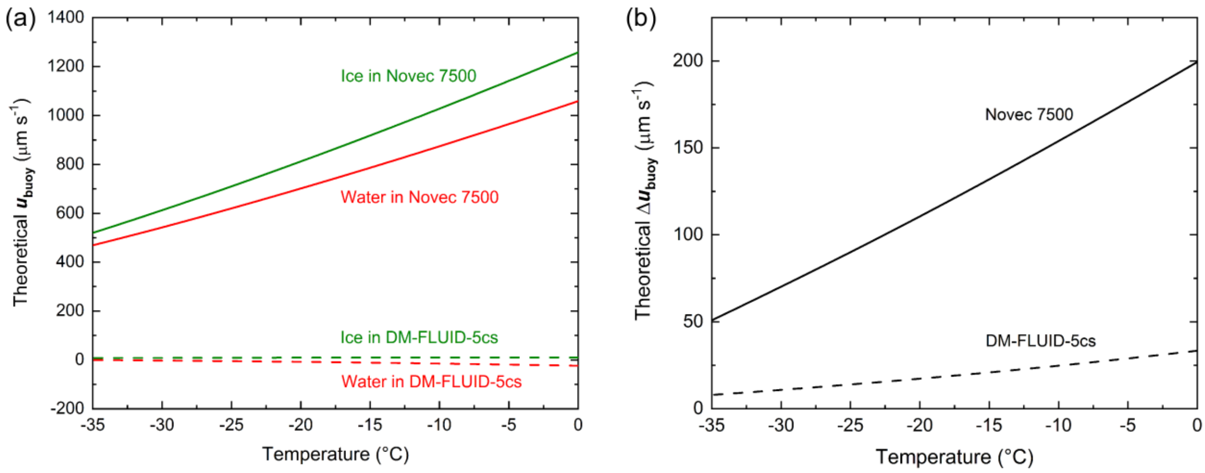

Fig. S11 (a) The theoretical velocities in the y-direction, $\boldsymbol{u}_{\mathbf{buoy}}$, of a water droplet and an ice crystal in Novec™ 7500 Engineered Fluid fluorinated oil (solid lines) and DM-FLUID-5cs silicone oil (dashed lines), based on the same parameters described in Fig. S10 for a water droplet of 115 μm diameter. The data for water and ice in Novec™ 7500 are the same as shown in Fig. S4. (b) The difference in theoretical $\boldsymbol{u}_{\mathbf{buoy}}$ values between a water droplet and ice crystal in Novec™ 7500 Engineered Fluid fluorinated oil and DM-FLUID-5cs silicone oil.

12. References

[1] B. J. Kirby, *Micro- and Nanoscale Fluid Mechanics: Transport in Microfluidic Devices*, Cambridge University Press, Cambridge, 2010.

[2] T. M. Squires and S. R. Quake, *Rev. Mod. Phys.*, 2005, **77**, 977-1026.

[3] K. W. Oh, K. Lee, B. Ahn and E. P. Furlani, *Lab Chip*, 2012, **12**, 515-545.

[4] F. M. White, *Fluid Mechanics, Seventh Edition*, McGraw-Hill, New York, 2011.

[5] J. Zhang, S. Yan, D. Yuan, G. Alici, N. T. Nguyen, M. Ebrahimi Warkiani and W. Li, *Lab Chip*, 2016, 16, 10-34.

[6] S. Dey, S. Z. Ali and E. Padhi, *Proc. R. Soc. A*, 2019, **475**, 20190277.

[7] E. Rabinovich and H. Kalman, *Powder Technol.*, 2008, **183**, 304-313.

[8] H. Kalman, D. Portnikov, O. G. Gabrieli, N. M. Tripathi, *Powder Technol.*, 2019, **354**, 485-495.

[9] J. Happel and H. Brenner, *Low Reynolds Number Hydrodynamics*, Noordhoff International Publishing, Leyden, 2nd Revised Edition, 1973.

[10] Y. Iiguni, M. Suwa and H. Watarai, *J. Chromatogr. A*, 2004, **1032**, 165-171.

[11] M. D. Tarn, N. Hirota, A. Iles and N. Pamme, *Sci. Technol. Adv. Mater.*, 2009, **10**, 014611.

[12] *3M™ Novec™ 7500 Engineered Fluid - Product Information* sheet, http://multimedia.3m.com/mws/media/65496O/3mtm-novectm-7500-engineered-fluid.pdf, 3M Company, accessed September 2019.

[13] A. Dehaoui, B. Issenmann and F. Caupin, *Proc. Natl. Acad. Sci. U.S.A.*, 2015, **112**, 12020.

[14] J. Hallett, *Proc. Phys. Soc.*, 1963, **82**, 1046-1050.

[15] A. F. Collings and N. Bajenov, *Metrologia*, 1983, **19**, 61-66.

[16] Y. A. Osipov, B. V. Zheleznyi and N. F. Bondarenko, *Russ. J. Phys. Chem.*, 1977, **51**, 748-749.

[17] D. E. Hare and C. M. Sorensen, *J. Chem. Phys.*, 1987, **87**, 4840-4845.

[18] *Properties of Ice and Supercooled Water*, in *CRC Handbook of Chemistry and Physics (CD-ROM Version 2010)*, 90th Edition, ed. D. R. Lide, CRC Press/Taylor and Francis, Boca Raton, FL, 2010, Chapter 6-12.

[19] H. R. Pruppacher and J. D. Klett, *Microphysics of Clouds and Precipitation*, Kluwer Academic Publishers, Dordrecht, 1997.

[20] S. J. La Placa and B. Post, *Acta Crystallogr.*, 1960, **13**, 503-505.

[21] D. C. Ginnings and R. J. Corrucini, *J. Res. Natl. Bur. Stand.*, 1947, **38**, 583-591.

[22] K. Y. Lonsdale and J. D. Bernal, *Proc. Royal Soc. A*, 1958, **247**, 424-434.

[23] D. Eisenberg and W. Kauzmann, *The Structure and Properties of Water*, Oxford University Press, Oxford, 1969.

[24] M. D. Tarn, S. N. F. Sikora, G. C. E. Porter, B. V. Wyld, N. Reicher, M. Alayof, A. D. Harrison, Y. Rudich, J.-u. Shim and B. J. Murray, *Lab Chip*, 2020, **20**, 2889-2910.

[25] C. S. Effenhauser, G. J. M. Bruin, A. Paulus and M. Ehrat, *Anal. Chem.*, 1997, **69**, 3451-3457.

[26] D. C. Duffy, J. C. McDonald, O. J. A. Schueller and G. M. Whitesides, *Anal. Chem.*, 1998, **70**, 4974-4984.

[27] J. C. McDonald, D. C. Duffy, J. R. Anderson, D. T. Chiu, H. Wu, O. J. A. Schueller and G. M. Whitesides, *Electrophoresis*, 2000, **21**, 27-40.

[28] Y. Kamijo and R. Derda, *Langmuir*, 2019, **35**, 359-364.

[29] *Shin-Etsu Silicone Fluid DM-FLUID Technical Data Sheet*, https://www.shinetsusilicone-global.com/catalog/pdf/kf96_us.pdf, Shin-Etsu Chemical Co., Ltd., accessed August 2020.